

Calibrating Column Density Tracers with Gamma-ray Observations of the ρ Ophiuchi Molecular Cloud

Ryan D. Abrahams^{1,2,3}, Alex Teachey^{4,5}, and Timothy A. D. Paglione^{1,2,3}

ABSTRACT

Diffuse gamma-ray emission from interstellar clouds results largely from cosmic ray (CR) proton collisions with ambient gas, regardless of the gas state, temperature, or dust properties of the cloud. The interstellar medium is predominantly transparent to both CRs and gamma-rays, so GeV emission is a unique probe of the total gas column density. The gamma-ray emissivity of a cloud of known column density is then a measure of the impinging CR population and may be used to map the kpc-scale CR distribution in the Galaxy. To this end, we test a number of commonly used column density tracers to evaluate their effectiveness in modeling the GeV emission from the relatively quiescent, nearby ρ Ophiuchi molecular cloud. We confirm that both HI and an appropriate H₂ tracer are required to reproduce the total gas column densities probed by diffuse gamma-ray emission. We find that the optical depth at 353 GHz (τ_{353}) from *Planck* reproduces the gamma-ray data best overall based on the test statistic across the entire region of interest, but near infrared stellar extinction also performs very well, with smaller spatial residuals in the densest parts of the cloud.

Subject headings: cosmic rays — gamma-rays: ISM — ISM: clouds — ISM: individual objects (ρ Ophiuchi)

¹Department of Physics, Graduate Center of the City University of New York, 365 Fifth Ave., New York, NY 10016, USA

²Department of Earth & Physical Sciences, York College, City University of New York, 94-20 Guy R. Brewer Blvd., Jamaica, NY 11451, USA

³Department of Astrophysics, American Museum of Natural History, Central Park West at 79th Street, New York, NY 10024, USA

⁴Department of Physics and Astronomy, Hunter College, City University of New York, New York, NY 10065, USA

⁵Department of Astronomy, Columbia University, 550 W 120th St., New York, NY 10027, USA

1. Introduction

Diffuse gamma-ray emission from the Milky Way informs us about the highest energy processes in the Galaxy such as supernova energy deposition, cosmic ray (CR) acceleration and energy losses, and CR transport. GeV gamma-ray emission in particular is a unique probe of hadronic CR processes. Specifically, CR protons and nuclei accelerated by supernova remnants impact ambient gas, which ultimately creates secondary pion emission with a characteristic spectral bump around 1 GeV (Ackermann et al. 2013). The interstellar medium (ISM) is effectively transparent to CRs, especially above the pion production threshold of 282 MeV. Therefore, interactions between lower energy CRs and molecular clouds can cause deep heating and ionization (Padovani et al. 2009), thus affecting cloud chemistry as well as star and planet formation (Glassgold et al. 2012; Indriolo & McCall 2012; Grenier et al. 2015). The higher energy interactions in turn give rise to gamma-ray emission sensitive to the total gas column density of a cloud independent of its dust properties, temperature, or gas state (HII, HI, or H₂).

Likelihood analyses of gamma-ray counts maps require modeling a variety of presumed emission sources including their spatial extents and spectral shapes. Typically, a number of gas templates based upon ISM tracers (21-cm HI emission, infrared dust emission, etc.), including one to account for molecular gas poorly traced by CO, the so-called “dark gas”, are compared to the gamma-ray emission. The differences between the observed gamma-ray counts maps and these templates often result in significant, spatially coherent residuals (e.g., Ade et al. 2015). These residuals are distinct from the dark gas and persist despite accounting for dark gas using dust maps or other measures. Given the goal of understanding the pervading CR density, spectrum, and its spatial variation through the Galactic disk, the distribution and column density of the gas with which CRs interact must be sensitively constrained. Common practice is to compare the gas templates to the gamma-ray counts, then incorporate any residual counts back into the templates to recover an ad hoc cloud emissivity from the gamma-ray data. Our goal instead is to reduce systematic uncertainties introduced by this method by identifying the best fitting cloud models based on maps of ISM tracers, and thus avoid distorting information about the underlying CR population.

We chose to study the ρ Oph molecular cloud because of its proximity to Earth ($d = 120^{+4.5}_{-4.2}$ pc) (Loinard et al. 2008) and relative quiescence, as well as for the many special features of the region that somewhat complicate the gamma-ray analysis. It has an estimated mass of $6.6 \times 10^3 M_{\odot}$ (Cambr  sy 1999) calculated from extinction measured via star counts to $1.2 \times 10^4 M_{\odot}$ (Yang et al. 2014) calculated from dust emission measured by the *Planck* satellite (Ade et al. 2011). The dust properties of the ρ Oph cloud are notoriously unusual (Liseau et al. 2015), which calls into question standard scaling relations

between A_V , A_λ , CO emission, dust emission, and gas column density. The ρ Oph dark core harbors the star-forming region L1688, which exhibits radio and X-ray emission (Dzib et al. 2013) potentially indicative of locally accelerated CRs. L1688 heats the dense part of the cloud, which can cause sharply varying dust temperatures that often complicate the dust modeling and column density determinations (Abergel et al. 2014). The molecular cloud is a known source of significant anomalous microwave emission (Ade et al. 2011), presumably an additional dust component. It also exhibits a high dynamic range in A_V , from widespread areas of $A_V < 1$ mag, to $A_V > 30$ mag near L1688. The diffuse gamma-ray emission from the cloud was studied with the *COS-B* and the *Compton Gamma-Ray Observatory* satellites (e.g., Issa & Wolfendale 1981; Hunter et al. 1994) and with the *Fermi Gamma-ray Space Telescope* (Yang et al. 2014). While at a relatively high latitude of $16^\circ 5'$, its proximity to the Galactic center line of sight implies significant gamma-ray contributions from Galactic inverse Compton (IC) emission, HI, gamma-ray point sources, and potentially HII. At least two bright and highly variable radio AGN, which are difficult to model appropriately and often leave large residuals, lie behind the diffuse cloud emission near L1688. Finally, the ρ Oph cloud lies in the immediate foreground of the northern *Fermi* bubbles (Su et al. 2010) as well as the Galactic center GeV excess (Daylan et al. 2016).

Assuming that gamma-rays are an unbiased and linear tracer of total gas column density, we test several gas templates based on emission and extinction measures to determine the systematic errors, biases, and appropriateness of each. Throughout this paper, we refer to the dense and extended complex of the ρ Oph molecular cloud as the ROMC to distinguish this feature from the B star ρ Ophiuchi itself.

2. Gamma-ray Data and Modeling

We use Pass 8 data from the *Fermi* LAT between August 4, 2008 and June 3, 2015. Pass 8 is the most recent data release from *Fermi* and improves upon photon detection and measurement, instrument point-spread function, and energy dispersion. Analysis of the gamma-ray data is performed with the *Fermi* science tools (v10r0p5) available from the *Fermi* Science Support Center ¹, utilizing both the P8R2_SOURCE_V6 and P8R2_ULTRACLEANVETO_V6 instrument response functions. When selecting the data, we consider both front and back converted photons in the “source” and “ultraclean veto” classes. These data classes differ in the strictness of background CR removal, where the ultraclean veto class has the lowest CR contamination. Both classes are analyzed separately to check for background systematics.

¹FSSC: <http://fermi.gsfc.nasa.gov/ssc/>

We downloaded data from a 15° radius around the chosen coordinates (RA, Dec = $246^\circ 4, -23^\circ 4$, J2000) and between 250 MeV and 10 GeV. The data were subsequently binned between $235^\circ 8 \leq \text{RA} \leq 257^\circ 0$ and $-34^\circ 0 \leq \text{DEC} \leq -12^\circ 8$ with a spatial resolution of 0.1 per pixel, and 30 logarithmically spaced energy bins between 250 MeV and 10 GeV. These energies are chosen to maximize both source localization and photon statistics. Including photons above 10 GeV does not improve the significance of the detection (Abrahams & Paglione 2015). We excluded photons with incidence angle $> 90^\circ$ from the zenith and any time the spacecraft rocking angle exceeds 52° . These constraints removed most gamma-ray contamination coming from the Earth’s limb. Figure 1 shows the gamma-ray counts map of the region.

The models analysed broadly consisted of two nearly independent components: point sources and diffuse sources. Point sources are taken from the 3FGL (Acero et al. 2015), and can be seen in Figure 1. Within the 3FGL point source catalog, a number of sources are included that are designated as “confused.” In general these sources are regions of excess emission that may not be associated with any known gamma-ray source. Toward L1688 there are two such sources, 3FGL J1628.2-2431c and 3FGL J1626.2-2428c, which appear to account for the gamma-ray emission from the densest part of the ROMC, and were therefore removed.

2.1. Diffuse Emission Templates

Diffuse components common to every model are: the isotropic emission, Galactic IC emission, and an H I map from the Galactic All-Sky Survey (GASS, Kalberla et al. 2010). In addition, we test an H II template (Finkbeiner 2003), as there are a number of hot stars in the region.

For the IC component, we used two different models calculated with GALPROP² (Strong & Moskalenko 1998; Vladimirov et al. 2011). One matches the older model used in Ackermann et al. (2012), and assumes a Galactocentric radius of 20 kpc, a maximum height between $|z| \leq 4$ kpc, the H II distribution from Cordes et al. (1991), and a parameterized CR source distribution given in the GALPROP manual as “source_model 1”. The second model assumes a larger CR halo with radius of 30 kpc, height $|z| < 6$ kpc, H II distribution from Gaensler et al. (2008), and a CR source distribution following the distribution of pulsars (Taylor et al. 1993).

The isotropic emission, originating from extragalactic diffuse gamma-ray emission and

²Source code can be found at <https://sourceforge.net/projects/galprop>

misclassified cosmic rays, is modeled by the “iso_P8R2_SOURCE_V6_v06.txt” or “iso_P8R2_ULTRACLEANVETO_V6_v06.txt” files provided by the Fermi Science Support Center. For the GASS HI map, the relevant portion of the sky coincident with the ROI was downloaded³.

Finally, the *Fermi* bubbles (Su et al. 2010) represent an additional background source of gamma-ray emission for the region. We assume a constant counts map across the ROI and the spectrum given in Ackermann et al. (2014).

2.2. Molecular Gas Templates

The following local ISM templates were compared to capture the molecular gas component, each model incorporated one of the following maps.

1. the standard *Fermi* Galactic diffuse model (Casandjian 2015a),
2. the 353 GHz dust optical depth, τ_{353} , from the *Planck* Public Data Release 1 (Abergel et al. 2014),
3. a map of the V -band extinction, A_V , constructed from data taken from DSS plates and using a star counts approach (Dobashi et al. 2005), which we will refer to as “Dobashi DSS,”
4. an A_V map constructed from 2MASS near-infrared (NIR) photometry using the so-called “X-percentile” method (Dobashi 2011), a modification of the Near-Infrared Color Excess (NICE) approach (Lada et al. 1994), and which we will refer to as “Dobashi 2MASS,”
5. our own A_V map using 2MASS photometry and the NICER technique as described in Lombardi & Alves (2001).

The *Fermi* diffuse model was used for comparison for the other models. Because the A_V tracer presumably traces both HI and H₂, it should account for most of the gamma-ray emission from the ISM. However, dust does not homogeneously trace both diffuse and dense regions in the ISM (Abergel et al. 2014). In addition, Peek (2013) showed that a combination of far infrared emission from dust and HI emission best reproduced the A_V . We therefore include both HI and A_V templates to more accurately trace the ISM.

³<https://www.astro.uni-bonn.de/hisurvey/gass/>

2.2.1. *Fermi* Galactic diffuse model

The *Fermi* Galactic diffuse model provided by the FSSC uses the LAB survey (Kalberla et al. 2005) to trace HI, the Dame et al. (2001) CO survey to trace molecular gas, and residual color excess from Schlegel et al. (1998) to trace dark gas. The residual color excess is found by subtracting a linear combination of the integrated intensities of HI and CO from the color excess.

2.2.2. *Planck* τ_{353}

The all-sky optical depth map at 353 GHz from *Planck*, τ_{353} , was downloaded from the NASA/IPAC Infrared Science Archive (IRSA) and the ROI extracted from the HealPix version 3.10 and converted to a Cartesian projection, shown in Figure 2. For comparison to the other extinction tracers, we converted τ_{353} to A_V assuming $A_V = 3.1E(B - V)$ and $E(B - V) = 1.49 \times 10^4 \tau_{353}$ (Abergel et al. 2014).

As described in Abergel et al. (2014), the dust opacity at 353 GHz is found by fitting a modified black body spectrum to the intensity detected by *Planck* at the frequencies of the High Frequency Instrument. The optical depth is proportional to the total column density of gas:

$$\tau_{353} = \sigma_{e,353} N_{\text{H}}, \quad (1)$$

where $\sigma_{e,353}$ is the dust emission opacity at 353 GHz, or roughly the optical depth per H atom, and is assumed to be constant in the *Planck* τ_{353} maps. Because τ_{353} traces dust and not total gas directly, this $\sigma_{e,353}$ factor depends on the gas-to-dust ratio, the dust optical properties, and the proportion of gas not traced by the N_{H} proxy (dark gas). Dark gas, which may be ionized gas, CO-faint- H_2 , optically thick HI, etc., serves to increase the $\sigma_{e,353}$ since there would be more gas, and thus also more dust emission, compared to N_{H} estimated from HI and CO emission.

We tested *Planck* maps of $E(B - V)$ and radiance as well, but their strong dependence on dust temperature makes them quite evidently inappropriate gas models, so we mostly omit them from subsequent analysis and discussion.

2.2.3. NICER

Another technique for deriving an A_V map using near infrared stellar colors, the NICER algorithm (Lombardi & Alves 2001) is capable of achieving a good dynamic range in A_V , especially in dense clouds (Alves et al. 2014; Lombardi et al. 2011). With the NICER approach, A_V is calculated using $J - H$ and $H - K_s$ colors from 2MASS and by comparing the median color excess of stars in a given map pixel to an intrinsic locus in color-color space estimated from a control region assumed to have $A_V = 0$. This method is successful because of the comparatively small scatter in intrinsic NIR colors and small variations in the extinction curve (Juvela & Montillaud 2016). Photometric errors are weighted such that more reliable colors carry more influence in the calculations. For this work we generated maps with $6'$ oversampled pixels to match the resolution of the *Fermi* maps. 2MASS photometry was downloaded from the IRSA website in four pieces to avoid data clipping associated with IRSA file size limits. We filtered the data using the `cc_flg` and `gal_contam` markers, thereby eliminating a variety of contaminated and confused sources, and in the final map we masked the bright star Antares which produces artificially high extinction measurements close to the ROMC. The map contained ~ 14 million stars after filtering. Stellar densities per pixel for this ROI range from < 10 up to > 1000 stars, with a median density ~ 130 stars per pixel.

To calculate the intrinsic locus of an extinction-free star sample, a reference field must be selected. As both stellar density and population compositions are dependent on Galactic latitude, we tested both large and small reference fields in three low-extinction regions of the map to quantify the effect of sample size and composition on the resulting map. The differences between the resulting maps were roughly 0.05 mag, which is an order of magnitude lower than the noise, indicating that the choice of control field sample size is largely negligible assuming the region is in fact nearly or entirely extinction-free. It is therefore suitable to select a fairly small region when observing sufficiently populated latitudes, as larger regions will necessarily sample a broader range of A_V . For our analysis we used a $6' \times 6'$ (1 pixel) reference field sample containing ~ 340 stars centered on $(\text{RA}, \text{Dec}) = (253^\circ.1, -27^\circ.1)$. The location of the reference field was also tested and is of particular importance for the ρ Oph region, which lies in front of the large stellar density gradient of the Galactic bulge. None of the extinction-free test fields resulted in differences in inferred cloud structures, only modest, $A_V < 0.4$ mag, systematic shifts in overall mean extinction over the entire ROI. Such a systematic shift in basically an extinction zero point has no effect on the renormalized templates used in the likelihood analysis, and we find no correlation with any cloud structures down to $A_V < 0.05$ mag. Maps generated with our code were compared with published maps of the ROMC (Ridge et al. 2006; Lombardi et al. 2008) as well as the Corona Australis dark cloud (Alves et al. 2014), and were found to be in good agreement.

2.2.4. Dobashi DSS

For the Dobashi extinction maps, only the relevant fraction of the sky coincident with our ROI was downloaded⁴. Dobashi et al. (2005) employed a traditional starcounts approach to generate A_V maps from the Digitized Sky Survey (DSS). Extinction was calculated using

$$A_\lambda(l, b) = \frac{[\log N_0(l, b) - \log N(l, b)]}{a_\lambda}, \quad (2)$$

where N is the observed stellar density, N_0 is the modeled background stellar density, λ is the band of the map, and a_λ is the slope of the $m_\lambda - \log N$ diagram, the so-called Wolf Diagram (Wolf 1923). As this method uses optical star counts, it is very sensitive to – but may also saturate at – relatively low values of A_V . Therefore, it is sensitive to the periphery of a dense cloud where $A_V \sim 1$ mag, but fails to properly probe the densest parts of the cloud due to low star counts.

2.2.5. Dobashi 2MASS

Dobashi (2011) developed an alternative to the NICE method for mapping extinction, the “X-Percentile Method”, utilizing 2MASS photometry. In this approach, the X^{th} percentile color excess is observed towards the cloud and compared to the X^{th} percentile color excess in a nearby reference field. Doing so corrects for foreground star contamination and the contamination from asymptotic giant branch stars and protostars, both of which are exceptionally red and can severely bias color excess measurements. While NIR photometry is not very sensitive to very low extinction regions, it allows more accurate values in dense clumps.

The final model may be written as

$$\begin{aligned} I(\ell, b, E) = & \sum_i PS_i(E) \delta_i(\ell, b) + x_{A_V} q_{\text{DMN}}(E) A_V(\ell, b) + x_{\text{HI}} q_{\text{HI}}(E) N(\text{HI}) \\ & + x_{\text{HII}} q_{\text{DNM}}(E) F_{\text{HII}}(\ell, b) + x_{\text{IC}} c_{\text{IC}}(\ell, b, E) \\ & + x_{\text{bubbles}} c_{\text{bubbles}}(E) + x_{\text{ISO}} c_{\text{ISO}}(E). \end{aligned} \quad (3)$$

⁴<http://darkclouds.u-gakugei.ac.jp/>

Each ISM component (A_V , HI, and HII) is multiplied by a gamma-ray emissivity, q_i , and a normalization x_i . We follow the naming conventions for the diffuse emissivities from Casandjian (2015b). The emissivities can be found in Table 1 of Casandjian (2015b) and were determined using Pass 7 Reprocessed data. This captures the general shape of the gamma-ray spectrum, which has remained relatively consistent from Pass 6 through Pass 7 Reprocessed, and even consistent with data from the COS-B and Compton Gamma-ray Observatory satellites (see Figure 4 of Casandjian 2015b).

2.3. Model Fitting Procedure

The model was convolved with the instrument response functions and exposure using `gtsrcmaps`. The result is fit to the data with the `gtlike` tool, which compares the observed gamma-ray counts to the number of gamma-ray photons predicted by the model. When fitting Equation 3 to the gamma-ray data, only the normalizations are varied. First we identify point sources with flux $> 10^{12}$ ph s $^{-1}$ MeV $^{-1}$ cm $^{-2}$ and those within 5° of the center of the ROI. We fix the normalizations for the diffuse components of the model and fit the normalizations for the identified point sources with the `gtlike` optimizer DRMNFB. Finally we fix the point source parameters and fit the normalizations for the diffuse sources. We repeated this procedure at least one additional time with the optimizer NewMinuit. After the second iteration, the fit parameters do not change significantly. This procedure exploits the fact that diffuse sources and point sources are generally uncorrelated spatially. Note that this assumption breaks down for 3FGL confused sources, which were removed for this analysis.

The basic procedure for the likelihood analysis of gamma-ray data is described in Cash (1979) and Mattox et al. (1996). To evaluate source detection and model significance, we consider the likelihood ratio statistic, which we call TS to match previous notation (e.g., Ackermann et al. 2012), which is proportional to the difference of the log likelihoods of two different models after each model is maximized over its parameters:

$$TS = -2 \left(\ln \mathcal{L}_A - \ln \mathcal{L}_B \right), \quad (4)$$

where \mathcal{L}_A and \mathcal{L}_B are the likelihoods for two models being compared (e. g., a source template versus a null). For each model, the combination of model parameters which maximizes that likelihood is found. The TS is related to the significance of model B over model A . The results do not change significantly if we consider a penalty on the addition of degrees of freedom, such as in the Bayesian information criterion (BIC; Schwarz 1978). This BIC adds

a penalty in the form of $+\Delta\nu \ln(n)$, where $\Delta\nu$ is the difference in the number of degrees of freedom between the two models, and n is the number of data points. Since models differ by at most four degrees of freedom, the TS would change by at most $4 \ln(30 \times 212^2) = 56$, where (30×212^2) is the number of bins in the counts cube, and the difference in the number of degrees of freedom represents the HI, HII, *Fermi* bubbles, and isotropic components.

However, this likelihood ratio only compares the overall fits to each other. Two models may have similar likelihoods while having structured residuals remaining. Therefore, we also compute residual maps and TS maps. A TS map is calculated by rastering a point source across the region and refitting the model. Each pixel in the resulting map represents the improvement in the overall likelihood due to the inclusion of the additional point source. Large, coherent structures in the TS map may represent unmodeled diffuse emission as opposed to unmodeled point sources.

3. Results and Discussion

3.1. Extinction Compared with Diffuse Gamma-ray Counts from the ISM

The total predicted counts for the 3FGL point sources, IC, and isotropic components may be subtracted from the counts map to render an estimation of the diffuse gamma-ray emission from the ISM alone (Figure 3). Figure 4 shows a pixel-by-pixel density plot of gamma-ray counts from the ISM versus A_V for four gas templates. We include only the central 10° of the gamma-ray data to focus on the ROMC and minimize the influence of the IC component close to the Galactic center.

Three of the tracers correlate reasonably well with the gamma-ray counts above $A_V \sim 0.5$ mag. The Dobashi DSS extinction does not reach above $A_V \sim 10$ mag, as expected due the limited optical star counts in highly extinguished areas. The scatter is larger and the correlation weaker for Dobashi 2MASS extinctions.

The τ_{353} and NICER extinctions correlate best with the gamma-ray counts, at least above $A_V \approx 1$ mag. There appears to be some nonlinearities below $A_V \approx 1$, close to the effective limit of both the *Fermi* and A_V data.

Despite their relatively good correlation, coherent and large-scale spatial differences between them are apparent in the maps. To highlight the differences between the two, we plot the difference $A_V(\tau_{353}) - A_V(\text{NICER})$ in Figure 5. Toward the highest integrated CO intensities, such as around L1688 and L1689, a higher A_V is estimated from τ_{353} than from NICER. These spots are coincident with 1.1 mm continuum sources (Young et al. 2006),

and may represent a bias in the τ_{353} maps. Some regions where the τ_{353} extinction is lower, such as around the star ρ Oph north of L1688, exhibit both elevated dust temperatures and lower dust emissivity power law indices (β), indicative of varying dust properties. These spots, however, may also suffer from a sampling bias in the NICER procedure. Sub-pixel scale structure, particularly toward highly extinguished areas, will preferentially allow starlight to pass through relatively diffuse gaps in the cloud, thus biasing the 2MASS extinctions downward. A stellar density map (Figure 6) confirms that these areas show marked decrements. Lombardi (2009) developed the NICEST algorithm to quantitatively address this issue, which we comment on further in a later subsection.

3.2. Model Component Contributions and Significance

Over the whole ROI, the gas components (A_V tracers) dominate the gamma-ray spectrum. While the A_V templates contribute to the gamma-ray emission more than the additional 21 cm template alone by over an order of magnitude, the HI component is still detected at a statistically significant level. This result suggests that the A_V map does not completely trace the ISM. HII also contributes less than an order of magnitude towards the total predicted gamma-ray counts, seen for both the NICER and the τ_{353} tracers in Fig 7. These spectra are integrated across the entire region. Both the A_V and IC components dominate the counts spectrum, while the isotropic component contributes an order of magnitude less. Both HI and HII components contribute significantly less than the A_V component. They are also spatially uncorrelated with the ROMC. Thus, we establish that A_V traces most of the diffuse gamma-ray emission from the ISM. However, HI and HII are still required when integrating across the entire ROI.

Table 1 lists the results from the gamma-ray likelihood analysis for the diffuse emission. The normalization for the IC contribution is notably high (greater than unity) in all cases. Although this may also indicate a poor choice of GALPROP inputs, it is unimportant to our discussion of the cloud structure given the lack of small-scale structure in the IC emission over the ROI.

The TS value listed in Table 1 compares each model to the *Fermi* diffuse model, where the baseline model analyzes the ULTRACLEAN VETO data class and includes: the IC from GALPROP galdef file “54 77Xvarh7S”, the isotropic component normalization fixed at unity, the *Fermi* bubbles, HI, and HII. Again, none of the models include the two confused point sources coincident with L1688. A positive TS value represents a better fit considering the entire ROI. It is important to note that for extended emission and large fields, judging the fit from this TS value alone can be misleading. In trying to determine

which gas template recovers the cloud emission best, we examine not only the TS value across the ROI, but also TS maps and residual maps, described below. Only the model with τ_{353} has a higher likelihood across the ROI than the *Fermi* diffuse model, with $TS = 89$. The higher TS stems almost entirely from accounting for the additional gamma-ray emission in L1688. The Galactic center excess, which is accounted for in the *Fermi* diffuse model, is another significant contributor to the likelihood differences when considering the entire ROI.

To quantify the importance of the various diffuse model components, we alternately modify each component in the model or change the gamma-ray data cut. We report the maximum percentage difference from the baseline model in Table 2. The dominant systematic uncertainty occurs when HI is not included in the model. The IC contribution in many cases is competitive with the A_V component, which is a consequence of its near isotropy over the ROI – it contributes to every pixel – and the strong expected IC signal towards the Galactic center. This is also seen in the predicted gamma-ray counts spectra in Figure 7. The other model components, such as the isotropic background and *Fermi* bubbles, contribute very little to the emission. In fact, the reduced photon statistics used to fit these components can make it difficult to spatially or spectrally distinguish them. The covariance matrix resulting from `gtlike` fits also indicates significant correlations between these weaker components.

3.3. Residual and TS Maps

The counts map is subtracted from the model generated from `gtmodel`, which which convolves the model with the exposure, point spread function, and instrument response function, to generate a residual map. Regions where the model underestimates the emission, then, result in a positive residual. Significance maps are generated by

$$\frac{N_{data} - N_{model}}{\sqrt{N_{model}}}. \quad (5)$$

The *Fermi* Galactic diffuse model, omitting the confused point sources 3FGL J1628.2-2431c and 3FGL J1626.2-2428c, produces a significant gamma-ray residual around L1688 (Figure 8). When included, these point sources have TS values of 305 and 189, and photon indices of -3.0 and -2.2 for the eastern and western sources, respectively. Such TS values indicate their significance. Their photon indices and lack of variability are typical for ISM emission. It is unclear why the *Fermi* diffuse model results in such a substantial residual at the CO emission peak of the ROMC, when it incorporates the Dame et al. (2001) CO map.

Figure 9 shows that τ_{353} and NICER perform significantly better – that is, have fewer and smaller spatially coherent residuals – than either Dobashi map, and better than the *Fermi* diffuse model near L1688. The NICER template underestimates the gamma-ray emission in the densest part of the ROMC, inside the western $W_{\text{CO}} = 50 \text{ K km s}^{-1}$ contour. The τ_{353} model overestimates the emission within the eastern $W_{\text{CO}} = 50 \text{ K km s}^{-1}$ contour near the L1689 cluster and the B star 22 Sco, and underestimates the gamma-ray emission just north of L1688 around the B star ρ Ophiuchi. Both of the Dobashi maps show significant, structured, positive and negative residuals across the entire ROI. These failures occur in both high and low density regions. The Galactic center excess is also seen in the southeast corner. While this signal is accounted for in the *Fermi* Galactic diffuse model, it is not included in our gas templates. It is thus a persistent residual in this study, but also physically distinct from the emission of the ROMC. τ_{353} reproduces the gamma-ray emission from the Galactic center region better than NICER or NICEST, which gives τ_{353} the highest TS value in Table 1

To further quantify the significance of the spatial residuals, we show TS maps for the *Fermi* diffuse model, NICER, and τ_{353} in Figure 10. The TS maps focus on the immediate region around L1688. The `gttsmap` routine places a point source at each pixel and evaluates its TS compared to the null. While the TS map can achieve higher resolution than the residual maps, the improvement of adding a point source can be assessed only if the original model underestimates the gamma-ray counts. The τ_{353} and NICER models used to make the TS maps include the HI component, but not the *Fermi* bubbles. Because the *Fermi* bubbles template is isotropic across the ROI, it does not affect the structure of the TS maps.

The TS map for NICEST shows the least structure, and thus it does not significantly underestimate the gamma-ray emission within the ROMC. The TS map for the *Fermi* diffuse model, τ_{353} , and NICER contain a regions of very high TS values near L1688, similar to its residual map. The τ_{353} model fails to the north of L1688 around the B star system ρ Ophiuchi (note again that the overestimate near L1689 is not captured in the TS map). The TS map for the NICER model primarily indicates a failure in the densest regions of the ROMC.

3.4. Cosmic Ray Sources in the ROMC

The NICER model appears to be the best overall fit for the ROMC based on the spatial residuals and integrated values of the TS maps. The lone residual appears in the densest part of the ROMC near L1688. An exciting possibility is that the young star-forming region could be a source of CRs, although a more likely explanation for the residual gamma-ray

signal is improper modeling of the ISM. As mentioned before, there is a known bias for photometric extinction methods to underestimate the column density towards dense regions. Indeed, the underestimate at L1688 is most severe for the Dobashi DSS template, which is expected given the quicker saturation of the optical extinction. Using the Dobashi DSS template, we insert a point source with a power law spectrum into the model at the location of L1688, which returns a TS value of 460, a photon index of -2.48 , and flux of 2.38×10^{-8} photons $\text{cm}^{-2} \text{ s}^{-1}$. We would expect a harder photon index from freshly accelerated CRs, but this putative source merely resembles the two confused 3FGL sources and typical ISM emission.

As mentioned before, small-scale cloud structure allows starlight to pass through relatively diffuse gaps in the clouds, thus causing a downward bias in extinction from the NICER and Dobashi methods. Lombardi (2009) found this effect to be most severe in the thickest regions of a cloud where there is a distinct decrease in star counts (Figure 6). In response, Lombardi (2009) developed the NICEST algorithm, which compensates for this bias using the star counts themselves.

To check for this bias, we model the gamma-ray observations from the ROMC with the NICEST map from Juvela & Montillaud (2016). The model excludes the *Fermi* bubbles. As shown in Figure 10, there are no significant gamma-ray residuals in the ROMC; the TS map shows no missing sources. Thus L1688 can be well modeled simply with diffuse emission templates. This result implies that L1688 is not an important local CR acceleration site. The NICEST extinction map yields the best recovery of the gamma-ray data of all the models tested in this study.

The *Planck* τ_{353} model underestimates the gamma-ray emission toward the ρ Ophiuchi star system, but overestimates the emission toward L1689 and 22 Sco. It may be that embedded hot stars alter the optical properties of the dust, causing a systematic offset in τ_{353} . The region of high TS for the τ_{353} model in Figure 10 is coincident with elevated dust temperatures (Figure 11). The locations of other embedded young stars, especially near L1688, similarly correspond to hot dust and variations in β (Figure 11). So while τ_{353} , including HI, seems to be a reasonable model in diffuse regions across the ROI, towards dense regions – especially those with embedded hot stars – the degeneracy between dust temperature and the dust spectral index may hamper its universality as a column density tracer.

4. Conclusions

We modeled the gamma-ray emission of the ROMC with different A_V tracers in order to determine which most accurately estimates column density in molecular clouds. Infrared dust optical depth at 353 GHz correlates well with the gamma-ray emission over the entire $20^\circ \times 20^\circ$ ROI, and even toward L1688, but may suffer some small systematic effects due to varying dust properties around embedded hot stars. Without correcting for the downward extinction bias caused by small-scale structure in very dense regions, the NICER method clearly underestimates the gamma-ray emission, and thus the column density, towards the dense core around L1688. The NICEST method attempts to correct for biases due to high extinction. As a result, NICEST most successively estimates the total gas column density as traced by the gamma-ray emission.

NICER, NICEST, and τ_{353} all suffer from noise constraints at low extinction, and thus cannot trace the ISM in low density regions. For NICER and NICEST, this is due to the intrinsic spread in stellar colors. τ_{353} suffers from uncertainties in modeling the infrared spectrum. The gamma-ray fit is improved significantly by including an HI component. This result verifies the claim that a combination of HI and far IR dust emission better traces A_V than either alone (Peek 2013).

We are able to recover all of the diffuse gamma-ray emission in the ROMC with templates based on gas or dust emission and/or extinction measurements. We find no evidence for any additional sources of CRs. Specifically, the young star cluster L1689 does not appear to be a significant CR acceleration site.

The authors thank the *Fermi* LAT team for their support. This work was supported in part by the NASA New York Space Grant Consortium based at Cornell University (#NNX10AI94H) and by the NSF (AST-1153335). Support for AT was provided by Undergraduate Research Fellowships and the Raab Presidential Fellowship at CUNY Hunter College. This research has made use of the NASA/IPAC Infrared Science Archive, which is operated by the Jet Propulsion Laboratory, California Institute of Technology, under contract with the National Aeronautics and Space Administration.

Facilities: *Fermi* (LAT)

REFERENCES

Abrahams, R. D. & Paglione, T. A. D. 2015, ApJ, 805, 50

- Abergel, A. and the *Planck* Collaboration. 2014, A&A, 571, A11
- Acero, F., Ackermann, M., Ajello, M. et al. 2015, ApJS, 218, 23
- Ackermann, M., Ajello, M., Allafort, A., et al. 2012b, ApJ, 755, 22
- Ackermann, M., Ajello, M., Allafort, A., et al. 2013, Science, 339, 807
- Ackermann, M., Albert, A., Atwood, W. B., et al. 2014, ApJ, 793, 64
- Ade, P. A. R., Aghanim, N., Arnaud, M. et al. 2011, A&A, 536, A20
- Ade, P. A. R. and the *Fermi* and *Planck* Collaborations. 2015, A&A 582, A31
- Alves, J., Lombardi, M. & Lada, C. J. 2014, A&A, 565, A18
- Cambr  sy, L. 1999, A&A, 345, 965
- Casandjian, J.-M. 2015a, 5th *Fermi* Symposium. Nagoya, Japan, 20 October 2014. arXiv:1502.07210
- Casandjian, J.-M. 2015b, ApJ, 806, 240
- Cash, W. 1979, ApJ, 228, 939
- Cordes, J. M., Weisberg, J. M., Frail, D. A., Spangler, S. R. & Ryan, M. 1991, Nature, 354, 121
- Dame, T. M., Hartmann, D., & Thaddeus, P. 2001, ApJ, 547, 792
- Dobashi, K., Uehara, H., Kandori, R., Sakurai, T., Kaiden, M., et al. 2005, PASJ, 57, S1
- Dobashi, K. 2011, PASJ, 63, S1
- Daylan, T., Finkbeiner, D. P., Hooper, D., et al. 2016, Physics of the Dark Universe, 12, 1
- Dzib, S. A., Loinard, L., Mioduszewski, A. J., et al. 2013, ApJ, 775, 63
- Finkbeiner, D. P. 2003, ApJS, 146, 407
- Gaensler, B. M., Madsen, G. J., Chatterjee, S. & Mao, S. A. 2008, PASA, 25, 184
- Glassgold, A. E., Galli, D., & Padovani, M. 2012, ApJ, 756, 157
- Grenier, I. A., Casandjian, J.-M., & Terrier, R. 2005, Science, 307, 1292
- Grenier, I. A., Black, J. H., & Strong, A. W. 2015, ARA&A, 53, 199

- Hunter, S. D., Digel, S. W., de Geus, E., J. & Kanbach, G. 1994, ApJ, 436, 216
- Indriolo, N., & McCall, B. J. 2012, ApJ, 745, 911
- Issa, M. R. & Wolfendale, A. W. 1990, ApJ, 354, 124
- Juvela, M. & Montillaud, J. 2016, A&A, 585, A38
- Kalberla, P. M. W., Burton, W. B., Hartmann, D., Arnal, E. M., Bajaja, E. et al. 2005, A&A, 440, 775
- Kalberla, P. A. M., McClure-Griffiths, N. M., Pisano, D. J., Calabretta, M. R., Alyson Ford, H. et al. 2010, A&A, 521, A17
- Lada, C. J., Lada, E. A., Clemens, D. P. & Bally, J. 1994, ApJ, 429, 694
- Liseau, R., Larsson, B., Lunttila, T., et al. 2015, A&A, 578, A131
- Loinard L., Torres R. M., Mioduszewski A. J., Rodríguez, L. F. 2008, ApJ, 675, L29
- Lombardi, M. & Alves, J. 2001, A&A, 377, 1023
- Lombardi, M., Lada, C. J. & Alves, J. 2008, A&A, 489, 143
- Lombardi, M. 2009, A&A, 493, 735
- Lombardi, M., Alves, J., & Lada, C. J. 2011, A&A, 535, A16
- Mattox, J. R., Bertsch, D. L., Chiang, J., Dingus, B. L., Digel, S. W. et al. 1996, ApJ, 461, 396
- Padovani, M., Galli, D., & Glassgold, A. E. 2009, A&A, 501, 619
- Peek, J. E. G. 2013, ApJ, 766, L6
- Ridge, N. A., Di Francesco, J., Kirk, H., Li, D., Goodman, A. A. et al. 2006, AJ, 131, 2921
- Schlegel, D. J., Finkbeiner, D. P., & Davis, M. 1998, ApJ, 500, 525
- Schwarz, G. E. 1978, Annals of Statistics, 6, 461
- Strong, A. W. & Moskalenko, I. V. 1998, ApJ, 509, 212
- Su, M., Slatyer, T. R., & Finkbeiner, D. P. 2010, ApJ, 724, 1044.
- Taylor, J. H., Manchester, R. N. & Lyne, A. G. 1993, ApJS, 88, 529

- Vladimirov, A. E., Digel, S. W., Jóhannesson, G., Michelson, P. F., Moskalenko, I. V. et al. 2011, *Computer Physics Communications*, 182, 1156
- Wolf, M. 1923, *Astronomische Nachrichten*, 219, 109
- Yang, R.-Z., de Oña Wilhelmi, E. & Aharonian, F. 2014, *A&A*, 566, A142
- Young, K. E., Enoch, M. L., Evans, N. J. II, Glenn, J., Sargent, A. et al. 2006, *ApJ*, 644, 326

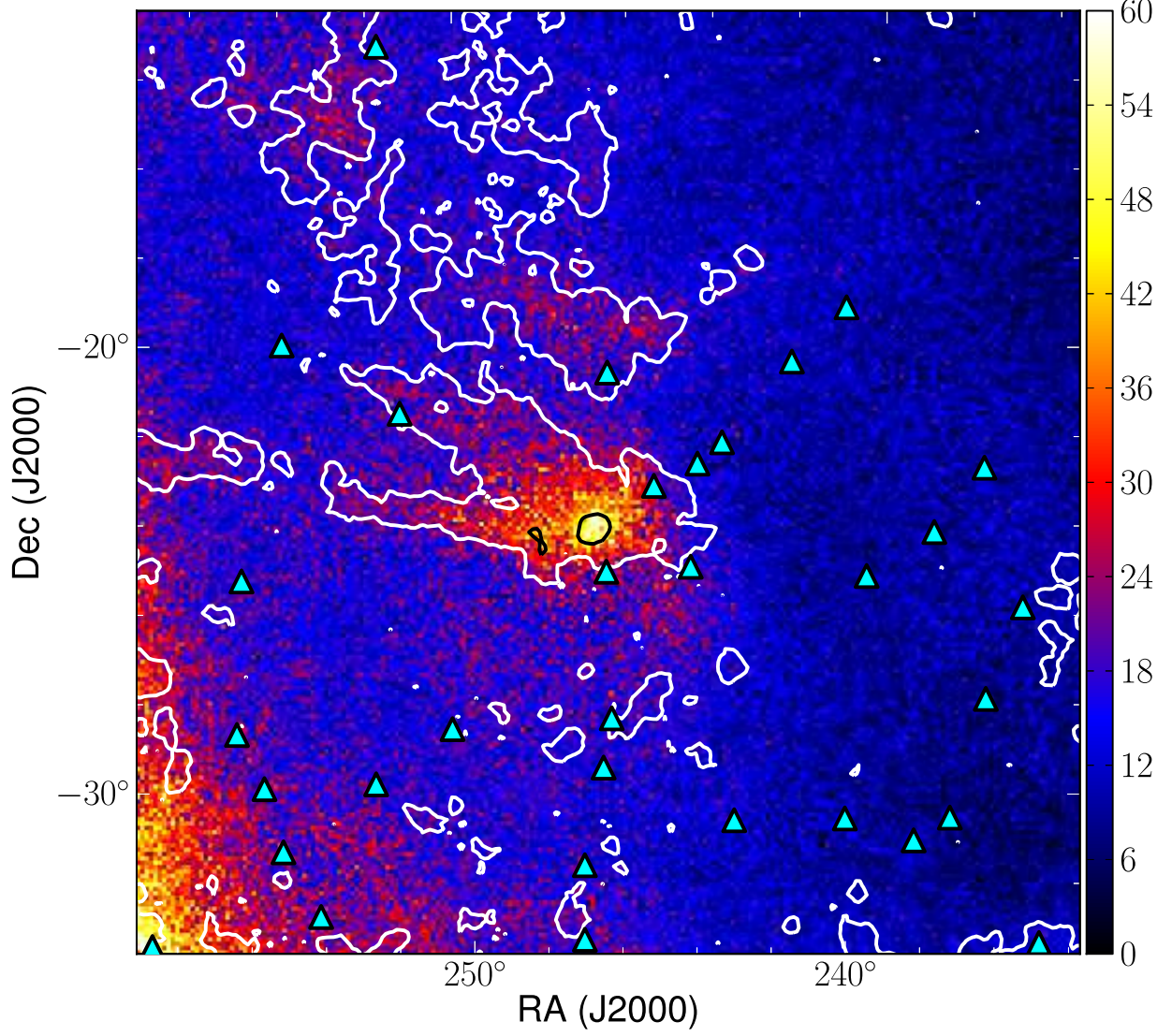


Fig. 1.— Gamma-ray counts map from 250 MeV to 10 GeV with 0.1° pixels centered on ρ Oph. White and black contours represent CO integrated intensities $W_{\text{CO}} = 2.5$ and 50 K km s^{-1} , respectively. The cyan triangles are 3FGL point sources included in the model.

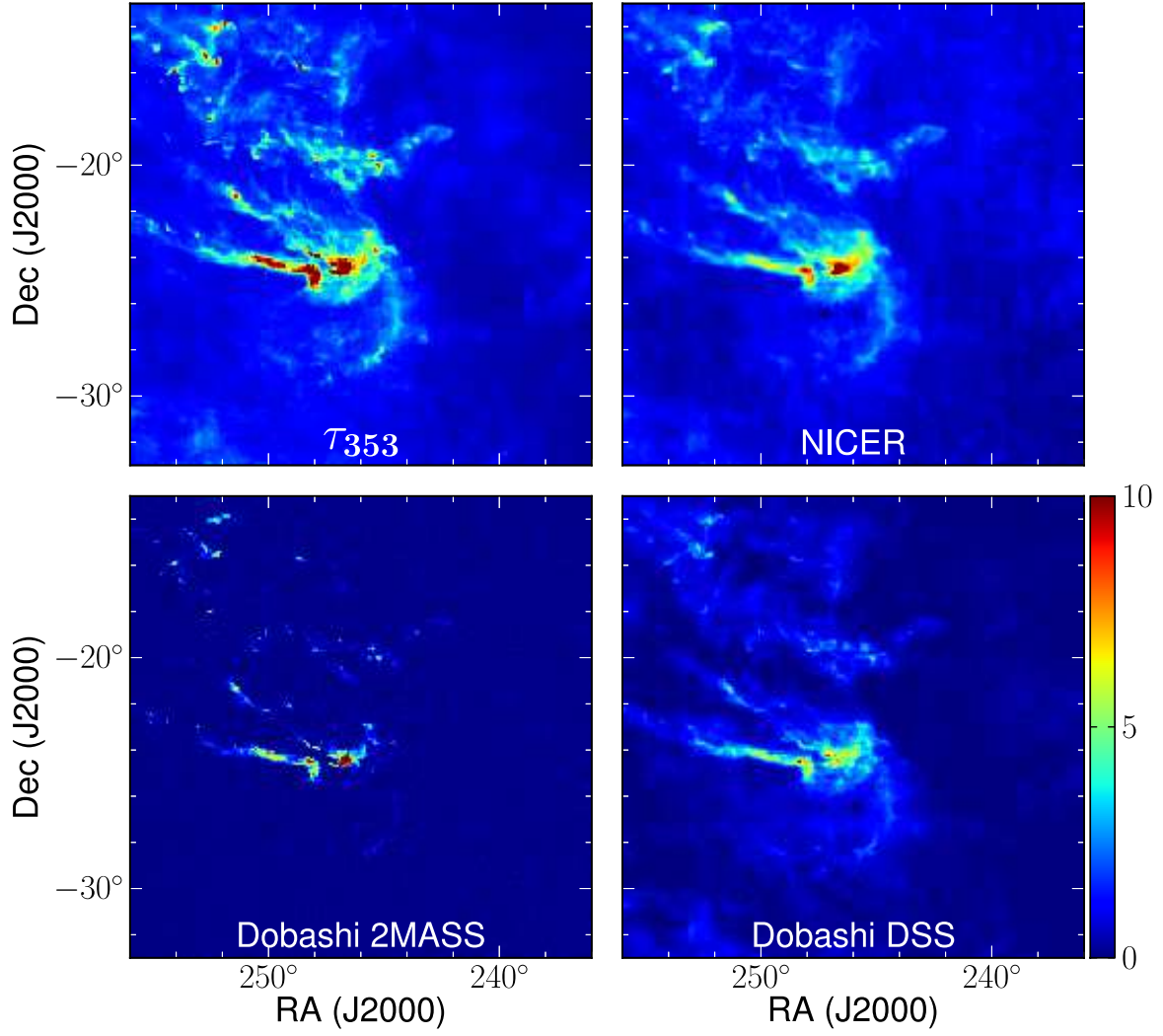


Fig. 2.— Column density tracer templates used for four of the models. Colors represent A_V and range from 0 to 10 mag of extinction.

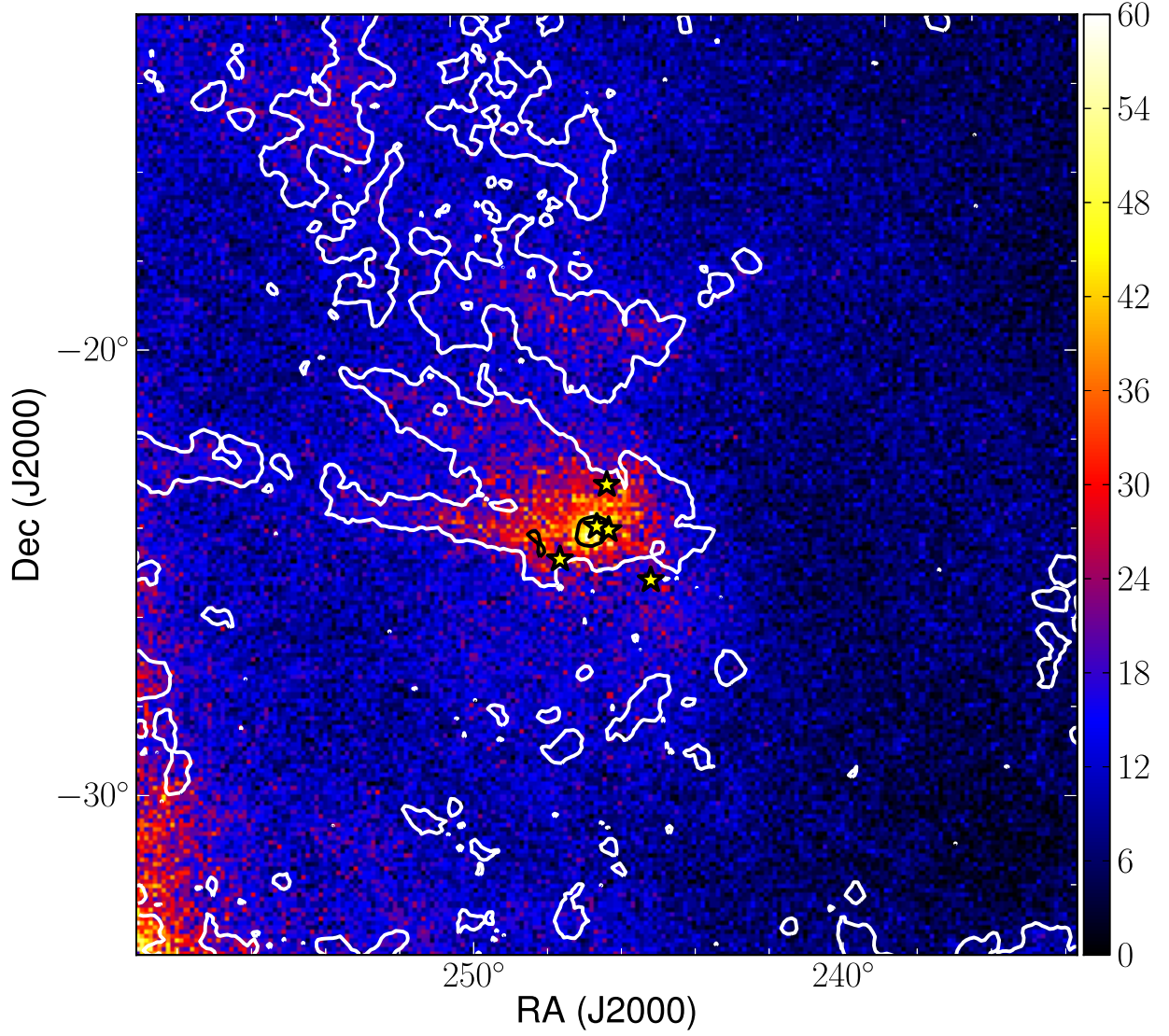


Fig. 3.— Total gamma-ray counts minus the predicted counts from point sources. Thus, the image shows a prediction for the diffuse gamma-ray emission. Contours are as in Figure 1, and the stars indicate B stars near the ROMC (from east to west: 22 Sco, S1, ρ Oph, HD 147889, σ Sco). The color scale is the same as Figure 1.

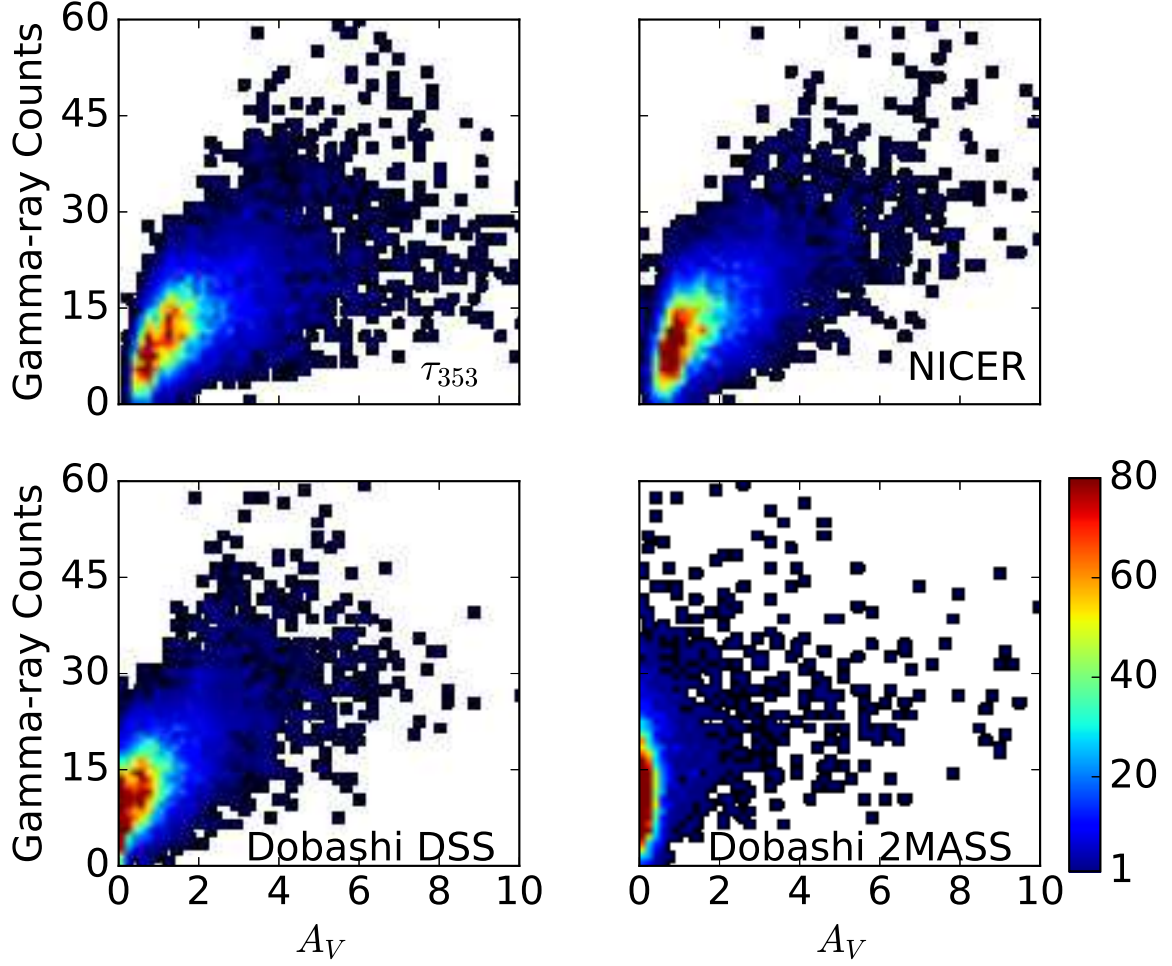


Fig. 4.— Diffuse gamma-ray counts from the ISM (central 10° of Figure 3) versus A_V tracers, where the color scale represents the number of pixels. The extinction is cut off at 10 mag in order to highlight the relationship at low extinction.

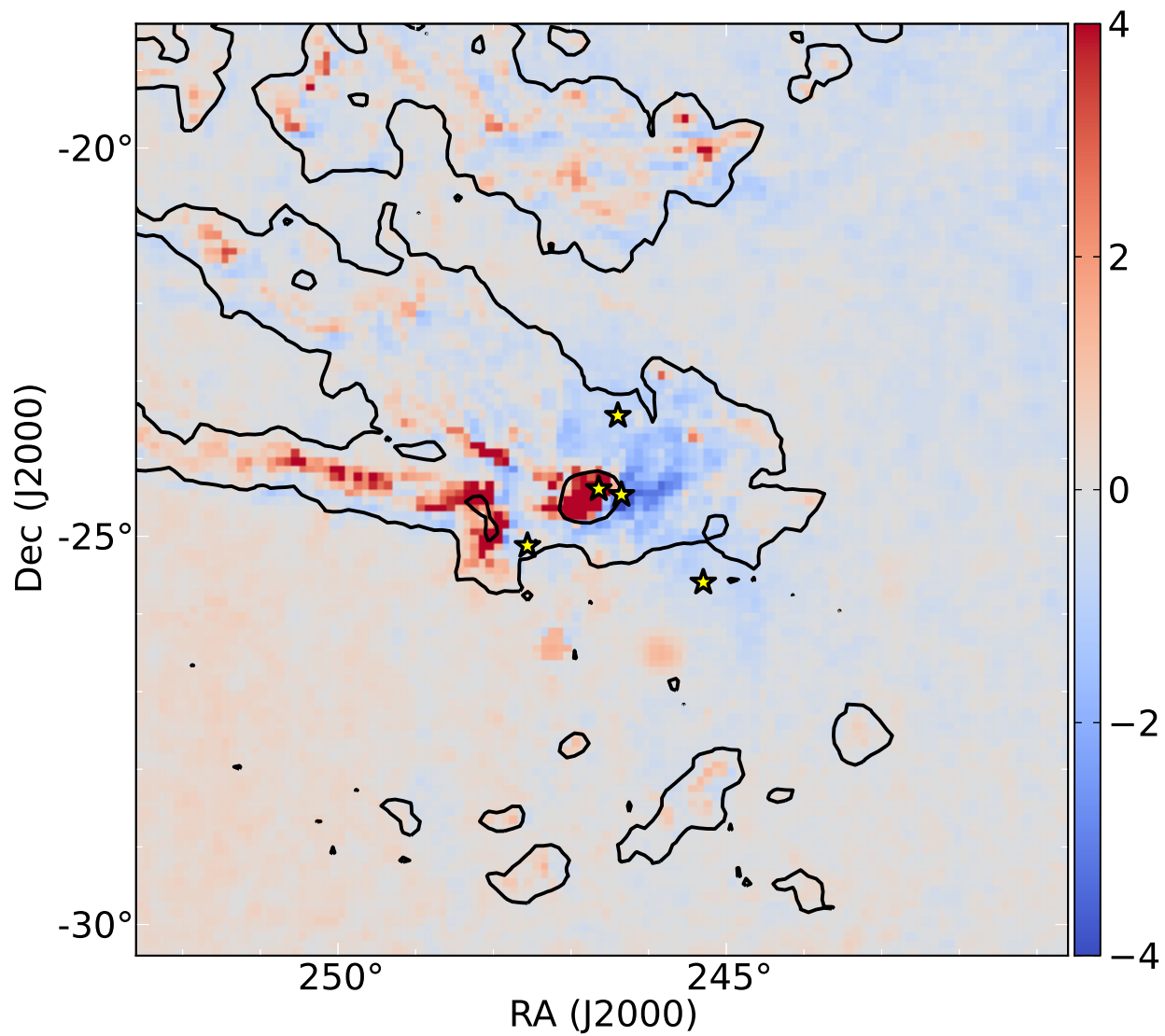


Fig. 5.— Difference of extinctions $A_V(\tau_{353}) - A_V(\text{NICER})$. $A_V(\tau_{353})$ is multiplied by 0.89 in order to match the low extinction regions and highlight the differences. Contours represent W_{CO} emission and symbols are nearby B stars, as described in Figure 3.

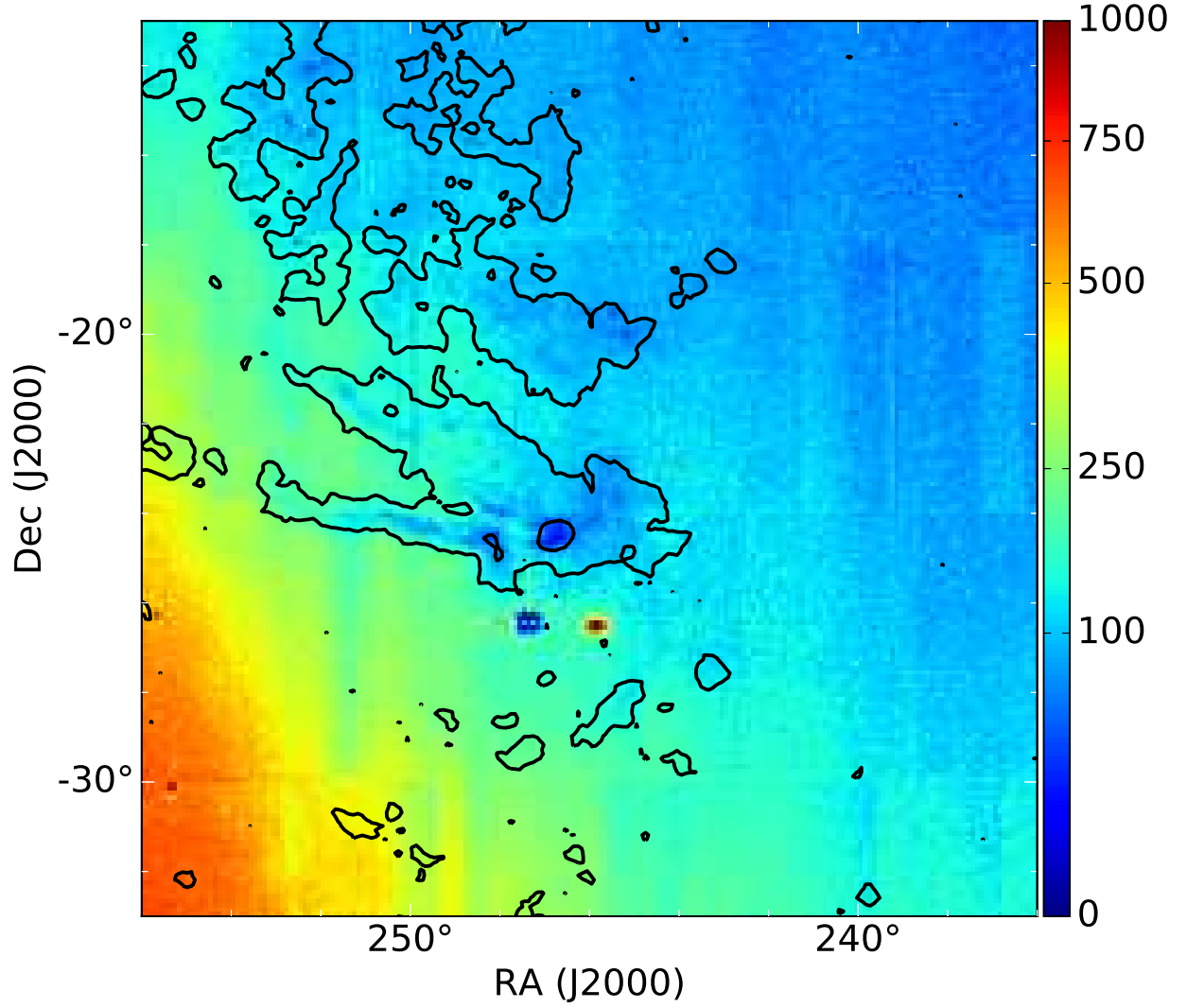


Fig. 6.— The number of 2MASS stars per 6' pixel. The ROMC can be seen as a relative deficit of stars with ≤ 100 stars per pixel. The blue circular feature just south of the ROMC is masked due to the bright foreground star, Antares at (247°3, -26°4). The density enhancement west of Antares is the globular cluster, M4 at (245°9, -26°5). Contours are as in Figure 1.

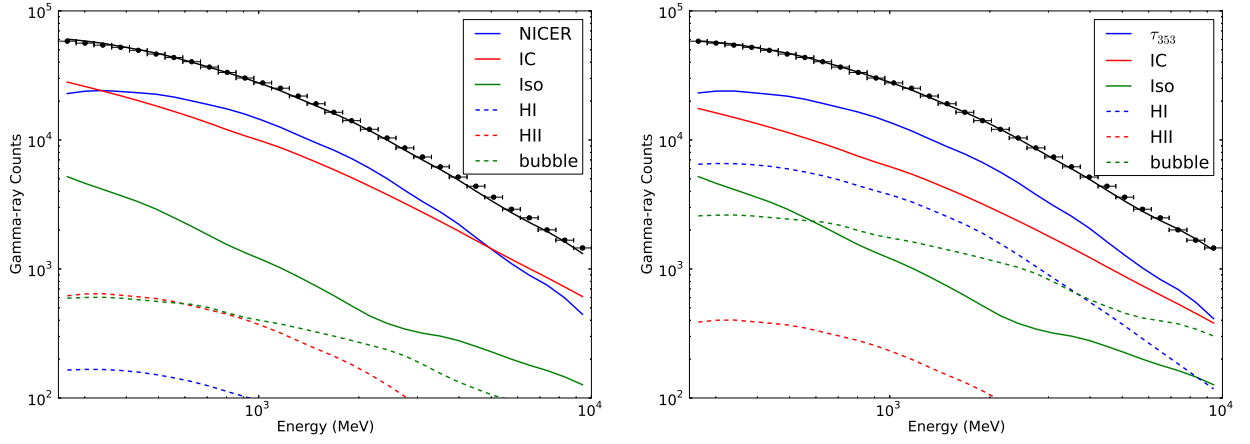


Fig. 7.— Observed versus predicted gamma-ray counts for the model and for diffuse components of the model for NICER (left) and τ_{353} (right). The black dots are the data and the black line is the sum of all model components. The A_V tracer and IC components dominate the integrated gamma-ray emission across the entire ROI.

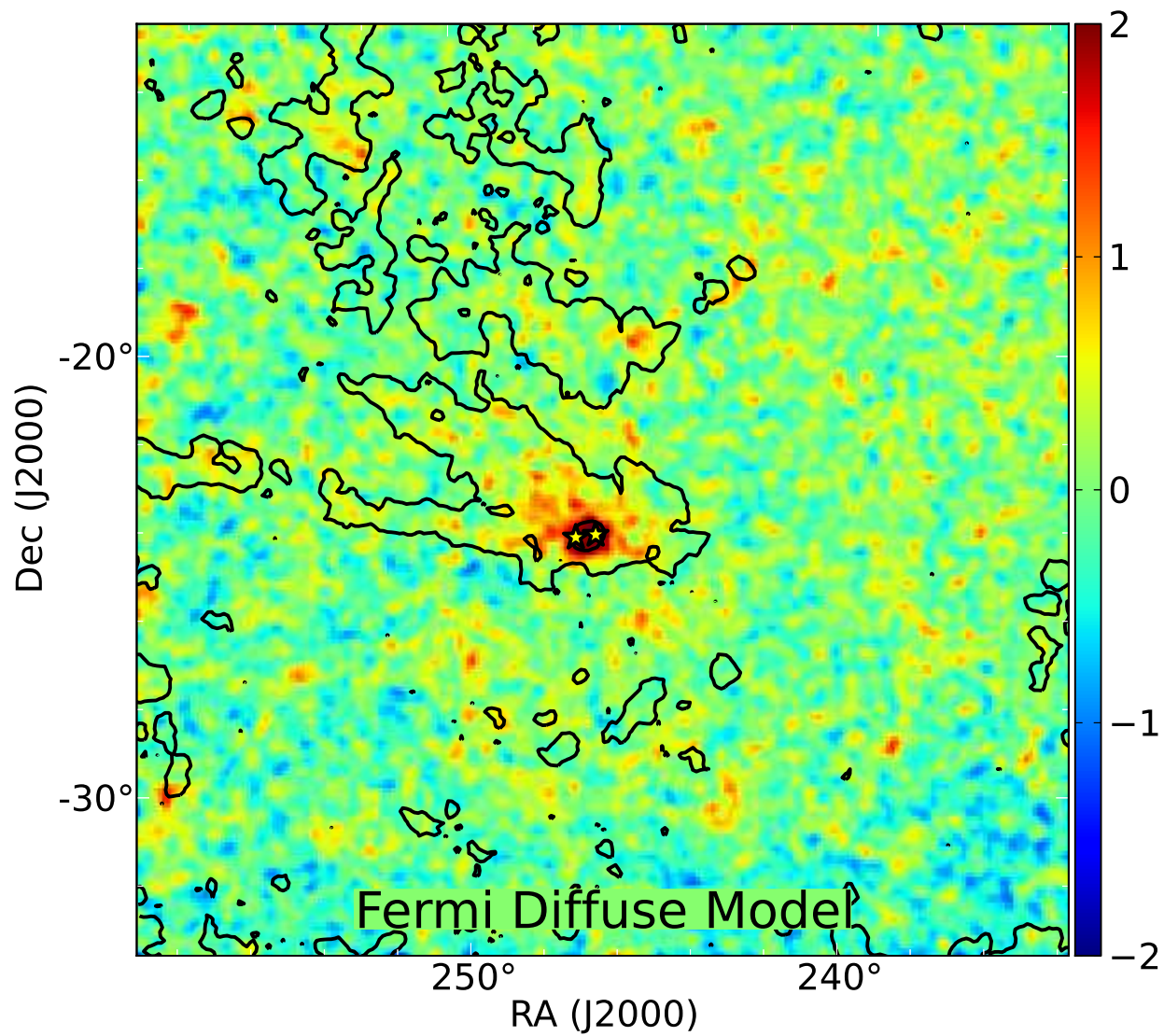


Fig. 8.— Residual significance map for the *Fermi* diffuse model smoothed with a 0.2° Gaussian kernel. The yellow stars mark the positions of the two confused point sources in the 3FGL, and contours are as in Figure 1.

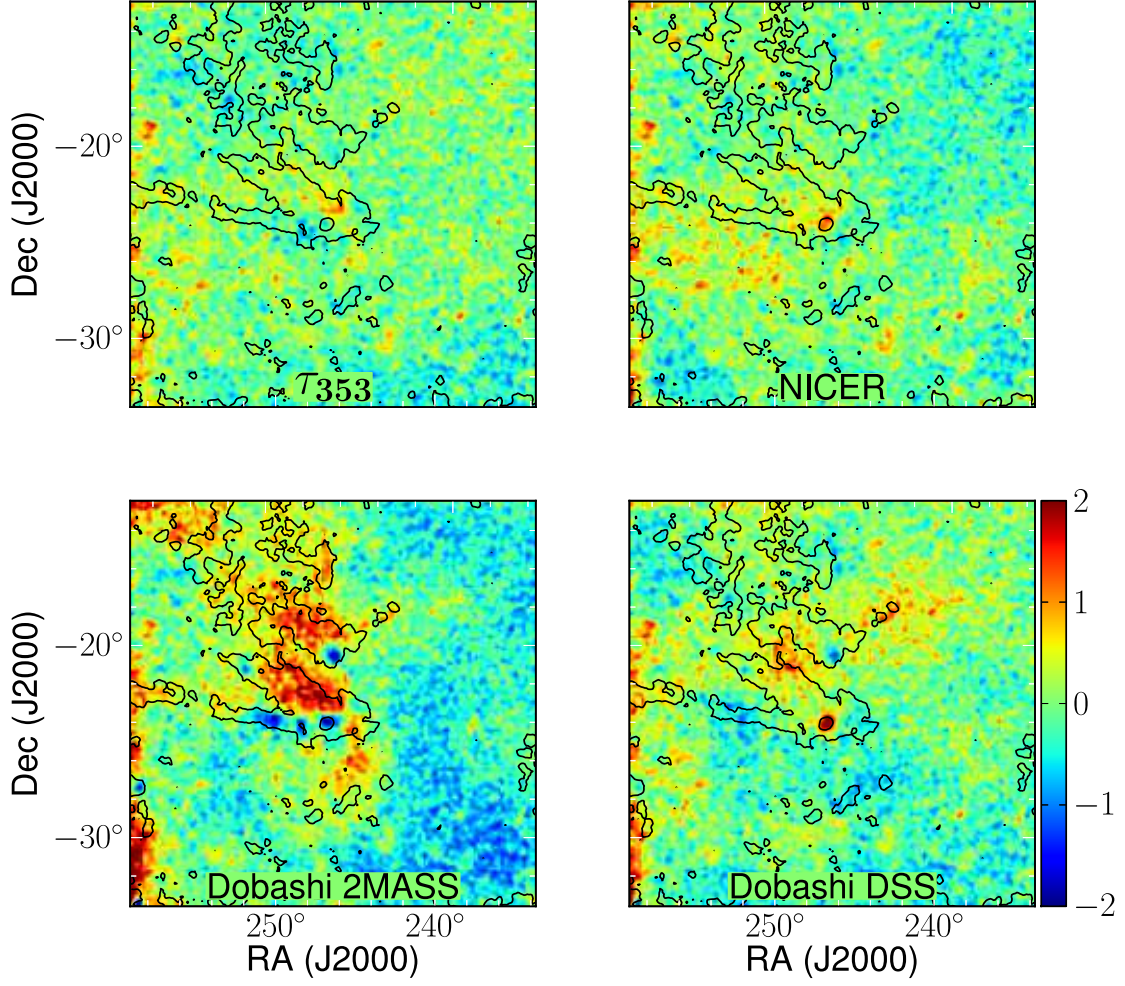


Fig. 9.— Residual significance maps for τ_{353} (top left), NICER (top right), Dobashi 2MASS (bottom left), and Dobashi DSS (bottom right) smoothed with 0.2 Gaussian kernel. Contours are as in Figure 1.

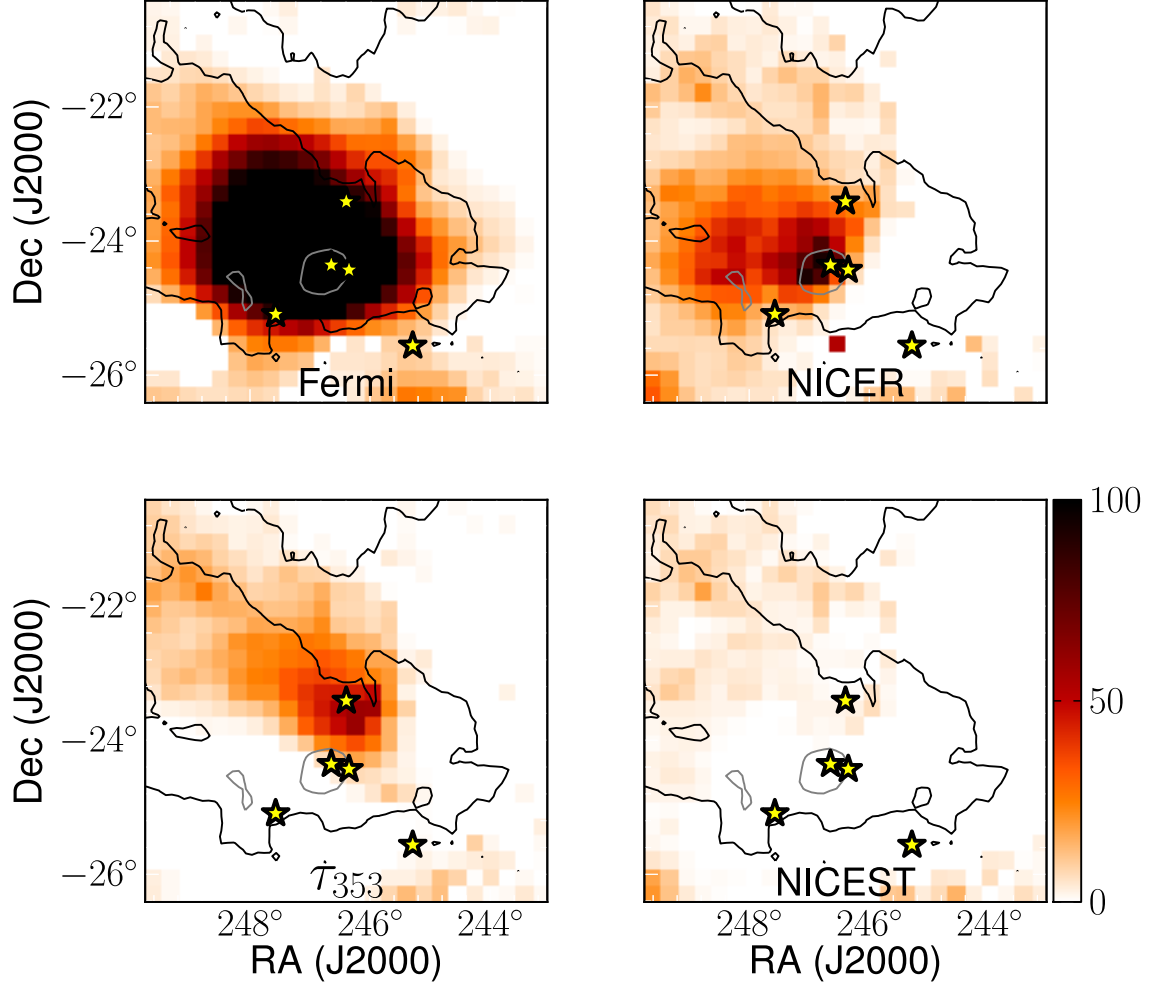


Fig. 10.— TS maps for the *Fermi* Galactic diffuse model (top left), the NICER extinction model (top right), the τ_{353} model (bottom left), and the NICEST extinction model (bottom right). All images have the same color scale. Contours and symbols are as in Figure 3.

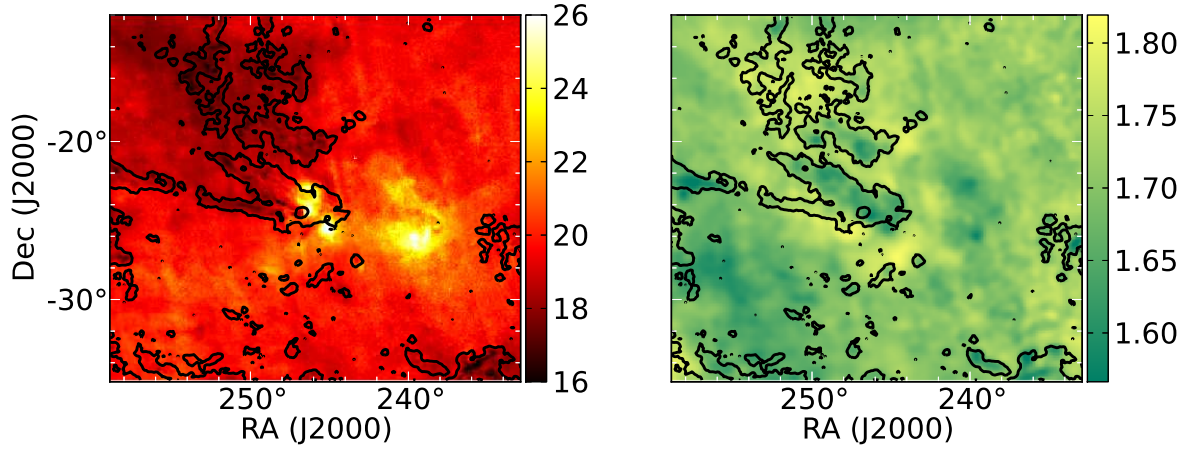


Fig. 11.— (Left) Dust temperature in K and (right) dust emissivity power law index β around the ROMC as determined by *Planck*. Contours are as in Figure 1.

Table 1. Results for extinction tracers

MODEL	TS^a	Normalization					
		A_V Tracer	H I	IC	Isotropic	Bubbles	H II
τ_{353}	89	1.06 ± 0.01	0.29 ± 0.02	2.34 ± 0.03	1	1.30 ± 0.05	$(3.91 \pm 0.67) \times 10^{-4}$
NICEST	-691	0.44 ± 0.01	0.13 ± 0.02	3.37 ± 0.03	1	0.80 ± 0.05	0.07 ± 0.01
NICER	-1609	0.43 ± 0.01	...	3.75 ± 0.02	1	0.30 ± 0.05	0.06 ± 0.01
Dobashi DSS	-3265	0.55 ± 0.01	1.10 ± 0.02	2.15 ± 0.03	1	1.57 ± 0.06	0.01 ± 0.01
Dobashi 2MASS	-12556	1.11 ± 0.01	1.34 ± 0.01	2.56 ± 0.03	1

Note. — The various dust tracers compared to the *Fermi* diffuse model and associated component normalizations ordered by TS .

^aModel likelihood for the entire ROI compared to the $-\ln \mathcal{L}$ of the *Fermi* diffuse model after removing the two point sources associated with the ROMC.

Table 2. Systematic Uncertainties

Model	Data Cut	IC Model	Iso free	Bubbles	H I	H II	Total
	(1)	(2)	(3)	(4)	(5)	(6)	(7)
τ_{353}	3.5	0.2	0.4	2.2	15.8	0.1	16.3
NICER	8.8	6.5	2.1	2.7	6.3	0.8	13.1
NICEST	5.9	3.9	0.1	0.8	9.5	0.1	11.9
Dobashi DSS	7.9	0.6	0.0	2.9	16.9	0.1	18.9
Dobashi 2MASS	11.9	5.7	2.6	4.9	57	1.7	58.8

Note. — Absolute value of the differences in A_V normalization among all models fitted for each A_V , as a percent difference from the baseline model. Column (1) Data Cut compares the SOURCE versus ULTRACLEAN VETO data cuts; Column (2) IC Model compares the two IC templates calculated from GALPROP; Column (3) Iso Free compares whether the isotropic component was fixed at one or set as a free parameter; Columns (4) – (6) compare the baseline model to those that omit the *Fermi* Bubbles, H I, or H II components, respectively; Column (7) Total is calculated by adding the other columns in quadrature.